



Microstructure and tailoring hydrogenation performance of Y-doped Mg_2Ni alloys



Wenjie Song, Jinshan Li, Tiebang Zhang*, Hongchao Kou, Xiangyi Xue

State Key Laboratory of Solidification Processing, Northwestern Polytechnical University, 127 Youyi Xilu, Xi'an 710072, PR China

HIGHLIGHTS

- Hydrogen storage capacity and kinetics of Mg_2Ni are improved with Y doping.
- Exploring the role of Y doping and melt-spun on the hydrogenation behavior of Mg_2Ni .
- Hydrogenation kinetics of melt-spun $\text{Mg}_{67}\text{Ni}_{33-x}\text{Y}_x$ are systematically analyzed.
- Hydrogenation mechanism of melt-spun $\text{Mg}_{67}\text{Ni}_{33-x}\text{Y}_x$ ribbons is proposed.

ARTICLE INFO

Article history:

Received 11 April 2013

Received in revised form

8 July 2013

Accepted 10 July 2013

Available online 18 July 2013

Keywords:

Hydrogen storage

Microstructure

Kinetics

Rapid solidification

Melt-spun

ABSTRACT

In this work, the microstructure and the hydrogenation properties of melt-spun $\text{Mg}_{67}\text{Ni}_{33-x}\text{Y}_x$ alloys are studied with the purpose to investigate the influence of Y doping and rapid solidification on hydrogenation performance of Mg_2Ni . $\text{Mg}_{67}\text{Ni}_{33-x}\text{Y}_x$ ($x = 0, 1, 3, 6$) alloys are firstly prepared in an electric resistance furnace under the protection of a covering reagent. Then, the as-cast alloys are re-melted and spun on a rotating copper roller. The phase compositions and microstructures of as-cast and melt-spun alloys are investigated by X-ray diffraction (XRD), scanning electron microscopy (SEM) with an energy dispersive spectrometer (EDS). The hydrogen activation properties and absorption/desorption kinetics of melt-spun $\text{Mg}_{67}\text{Ni}_{33-x}\text{Y}_x$ ($x = 0, 1, 3, 6$) ribbons are evaluated using an automatic Sieverts apparatus. The melt-spun $\text{Mg}_{67}\text{Ni}_{32}\text{Y}$ alloy preserves high hydrogen absorption capacity and kinetics and absorbs 96% of the maximum capacity (3.79 wt. %) within 8 min. The lattice distortion caused by Y doping and the shrinkage porosity by melt-spun not only raise the hydrogen absorption/desorption rate, but significantly improve the hydrogen storage capacity of $\text{Mg}_{67}\text{Ni}_{33-x}\text{Y}_x$ ($x = 0, 1, 3, 6$) alloys. The activation and hydrogen absorption/desorption mechanisms are also discussed based on a nucleation and growth theory.

© 2013 Elsevier B.V. All rights reserved.

1. Introduction

The demand of renewable clean energy is rising due to environmental concerns of the harmful emissions from the fossil fuels used presently and the shortage of traditional power sources [1,2]. Hydrogen's physical and chemical advantages make it an important energy carrier in the future [3]. Developing safe, efficient and cost-effective hydrogen storage technologies is a key challenge for hydrogen economy [3–5]. With the fact that metals and alloys are capable of reversibly absorbing hydrogen, a

large hydrogen storage capacity and the safe mean of hydrogen storage (comparing with liquid hydrogen and high-pressure hydrogen storage), the metal hydrides are considered as an ideal medium of hydrogen storage for on-board vehicle applications [3,4,6].

Magnesium and magnesium-based alloys are particularly considered as attractive and promising hydrogen storage materials for the solid-state storage of hydrogen due to the high theoretical storage capacity (7.6 wt. % for Mg), light weight, abundant resources, low environmental impact and low cost. However, the high working temperatures and the slow hydrogen absorption and desorption kinetics prevent Mg and Mg-based alloys from practical applications [5,7]. During past decades, a great deal of effort has been devoted to overcome these obstacles and improve the hydrogen storage properties. Generally, the strategies for improving the hydrogen absorption kinetics of magnesium-based

* Corresponding author. Tel.: +86 29 88491764; fax: +86 29 88460294.
E-mail address: tiebangzhang@nwpu.edu.cn (T. Zhang).

alloys can be divided into two categories [5,8]. One is the preparation of an ultra-fine microstructure with the help of mechanical alloying (MA) [9], cold rolling [10], hydriding combustion synthesis [11], vapor deposition [12], equal channel angular pressing [13] and melt-spun [5]. The other is the addition of alloying element (e.g. transition metals [14] and rare earth (RE) metals [5,15]) or catalytic components. Carbon structure materials [16], halogenide [17], transition metal oxides [18] and other hydrides [19] are usually used as catalysts in Mg-based alloys to enhance the hydrogen absorption kinetics and capacity. The alloying elements and catalysts have been proven to decrease the temperature of hydrogen absorption/desorption and ameliorate the kinetics on various degree.

The metal substitutions have an positive effect on the absorption/desorption kinetics of Mg. Comparing with pure Mg, the Mg₂Ni alloy shows higher kinetics and lower hydrogen absorption/desorption temperature, which can be mainly attributed to the catalytic effect of Ni [20]. However, the hydrogen storage capacity of Mg₂Ni decreases comparing with that of pure Mg. It has been reported that the addition of rare earth elements including Y, La, Nd, Ce and mischmetal into Mg and Mg-based alloys ameliorate the hydrogen absorption and desorption kinetics [7,21–23]. Kalinichenka et al. [21] report that yttrium can be solved in Mg₂Ni and results in a lattice expansion, the Mg–Ni–Y alloy exhibits higher dehydrogenation rates comparing with that of the Mg–Ni alloy. Shang and co-workers [22] find that MgH₂ mixed with Y and Ce by mechanical milling increases desorption kinetics and decreases desorption temperature comparing with that of pure MgH₂. Nd adding into Mg₂Ni alloy also enhances the hydrogen absorption kinetics significantly [7]. Rare earth metal hydrides have been proven to preserve significant catalytic effect on the hydrogen absorption–desorption reactions in the Mg–H₂ system [24]. Rare earth metal is beneficial to increase the hydrogen absorption/desorption kinetics and decrease the temperature of Mg₂Ni-based alloys. Up to now, both the sluggish kinetics and high hydrogen absorption/desorption temperature are still obstacles for application of Mg and Mg-based alloys. The single alloying method is not sufficient to overcome the obstacles. It is necessary to explore new technique equipped with the aforementioned alloying method to further improve the hydrogen absorption–desorption kinetics and capacity of Mg-based alloys for practical applications. Considering the possible catalytic effect of rare earth metal hydrides and the fact that the rapid solidification can significantly reduce the grain size, the substitution of Ni by Y and the melt-spun technique can be expected to improve the hydrogen absorption/desorption capacity and kinetics of Mg₂Ni.

The microstructure and tailoring hydrogenation properties of Y-doped Mg₂Ni alloys are discussed in this work. It is expected to reveal the effects of doping Y and rapid solidification on microstructure and hydrogen absorption/desorption behaviors of the melt-spun ribbons, as well as the relation between microstructure and hydrogenation/dehydrogenation properties. In this work, phase compositions and microstructures of as-cast and melt-spun Y-doped Mg₂Ni alloys are characterized by XRD and SEM with EDS. Lattice parameter and microstructures of experimental alloys are compared with various Y content. The microstructure evolution with different compositions of as-cast and melt-spun alloys are analyzed. The formation of as-cast and melt-spun microstructures is analyzed by the solidification theory. The effect of the shrinkage porosity in melt-spun alloys on activation and hydrogen absorption/desorption processes are studied in this work. The activation and hydrogen absorption/desorption mechanisms are discussed based on the nucleation and growth theory.

2. Experimental

2.1. Materials preparation

The Mg₆₇Ni_{33–x}Y_x ($x = 0, 1, 3, 6$ atom%) alloys were melted in the graphite crucible in an electric resistance furnace under the protection of the covering reagent. The composition of the covering reagent is 44 wt. % MgCl₂, 44 wt.% KCl, 7 wt. % BaCl₂ and 5 wt. % CaF₂. Commercial purity magnesium ingot (purity 99.9%), magnesium–yttrium intermediate alloy (the content of Y is 30 wt. %, purity 99.9%) and nickel powders (purity 99.99%) were used as raw materials. Nickel powders were cold pressed on an electric tablet machine at pressure 1.5 ton and holding 30 s. Considering the inherent evaporation effect of elements during melting, 5 wt. % of Mg and 2 wt. % of Y were added as the estimated melting loss, respectively. The melting process was divided into two steps, magnesium and magnesium–yttrium intermediate alloy were heated to molten state completely, then Ni tablets were put into liquid. Ni tablets were dispersed quickly under the action of thermal shock. In order to make all the metals fully melted and homogeneously mixed, the molten alloy was kept at 1023 K for 30 min and stirred to ensure the homogeneousness. It is important that alloys must be protected by the covering reagent during the melting process. The as-cast alloys were finally obtained as the liquid alloys cooled down to room temperature in the graphite crucible. The as-cast alloys were preserved in super purified glove box after the covering reagent removed. The as-cast alloy was remelted and spun on a rotating single roller in an argon atmosphere of 500 mbar. The linear velocity of the casting wheel was 40 ms^{–1}. The melt-spun ribbons were about 50 μ m in thickness and 5 mm in width, the length was about 10–30 mm.

2.2. Characterization and measurement

The phase compositions and structures of the as-cast alloys were determined by an X-ray diffractometer (DX-2007) with Cu K α radiation. The X-ray patterns were collected between a diffraction angle (2θ) 15–90° with a velocity of 0.03° per seconds. The voltage and the current are 35 kV and 35 mA, respectively. Scanning electron microscopy (SEM) equipped with an energy dispersive X-ray spectrometer (EDS) was employed to characterize the microstructure and the corresponding chemical composition.

The activation and hydrogen absorption/desorption behaviors of the melt-spun ribbons were measured using a Sieverts apparatus PCT Pro2000. The activation entailed 3 hydrogenation and dehydrogenation cycles. During the activation process, the melt-spun ribbons were firstly hydrogenated in an initial hydrogen pressure 30 bar for 10 h at 623 K, and then dehydrogenated in vacuum for 1 h at 623 K. The hydrogen absorption kinetics and capacity were measured in a hydrogen pressure of 30 bar at 573 K, the hydrogen desorption was measured in vacuum at the corresponding absorption temperature.

3. Results and discussion

3.1. Phase structure of as-cast and melt-spun Mg₆₇Ni_{33–x}Y_x

The XRD patterns of the as-cast Mg₆₇Ni_{33–x}Y_x ($x = 0, 1, 3, 6$) alloys are shown in Fig. 1. The dominant phase of each as-cast experimental alloy can be ascribed to Mg₂Ni phase. Several Bragg peaks of α -Mg and MgNi₂ are also observed in the XRD patterns of the as-cast Mg₆₇Ni_{33–x}Y_x alloys with $x = 0$ and 1. With the increase of Y content, the Bragg peaks of MgYNi₄ are also observed in alloys with $x = 3$ and 6 in addition to the Mg₂Ni and α -Mg phases. Judging from the Mg–Ni phase diagram, the MgNi₂ phase firstly

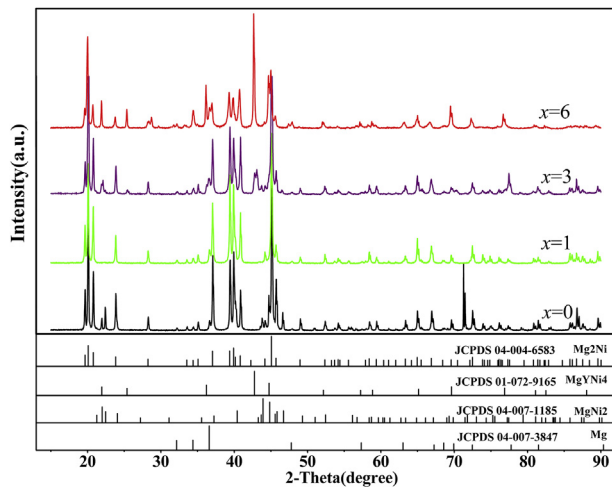


Fig. 1. XRD patterns of the as-cast $\text{Mg}_{67}\text{Ni}_{33-x}\text{Y}_x$ ($x = 0, 1, 3, 6$) alloys.

precipitates from liquid during the solidification process, then the peritectic reaction $\text{L} + \text{MgNi}_2 \rightarrow \text{Mg}_2\text{Ni}$ occurs [25]. The peritectic reaction is normally incomplete at the normal solidification condition, a small quantity of MgNi_2 phase is always retained in the as-cast alloys [26]. With the further decrease of temperature, the eutectic reaction $\text{L} \rightarrow \text{Mg}_2\text{Ni} + \text{Mg}$ occurs in the remnant liquid. From the Mg-Ni-Y phase diagram, the MgYNi_4 phase is tend to be formed in Mg-Ni alloy with the addition of Y [27]. The MgYNi_4 phase is not detected in the as-cast $\text{Mg}_{67}\text{Ni}_{33-x}\text{Y}_x$ with $x = 1$ alloys within the resolution of XRD. With increasing Y , MgYNi_4 with C15b (AuBe_5)-type Laves phase structure [28] is observed in the as-cast $\text{Mg}_{67}\text{Ni}_{33-x}\text{Y}_x$ alloys with $x = 3$ and 6.

The Rietveld refinements for the XRD patterns of the melt-spun $\text{Mg}_{67}\text{Ni}_{33-x}\text{Y}_x$ ($x = 0, 1, 3, 6$) ribbons are shown in Fig. 2. Only Bragg peaks of Mg_2Ni and Mg phases are observed in the melt-spun $\text{Mg}_{67}\text{Ni}_{33-x}\text{Y}_x$ ribbons with $x = 0$ and 1. The MgYNi_4 phase is also

contained in the melt-spun ribbons with $x = 3$ and 6 in addition to Mg_2Ni and $\alpha\text{-Mg}$ phases. The MgNi_2 phase without hydrogen absorption capacity can be eliminated from the $\text{Mg}_{67}\text{Ni}_{33-x}\text{Y}_x$ alloys with $x = 0$ and 1 by melt-spun technique. The lattice parameters, unit cell volumes and the corresponding volume fraction of each phase are listed in Table 1. With the increase of Y content, the fraction of Mg_2Ni decreases from 97.4 wt. % for the alloy with $x = 0$ –88.5 wt. % for the alloy with $x = 6$. Meanwhile, the content of $\alpha\text{-Mg}$ increases from 2.6 wt. % for the alloy with $x = 0$ –7.3 wt. % for the alloy with $x = 6$. The content of MgYNi_4 in the $\text{Mg}_{67}\text{Ni}_{30}\text{Y}_3$ and $\text{Mg}_{67}\text{Ni}_{27}\text{Y}_6$ ribbons is 2.5 wt. % and 4.2 wt. %, respectively. The increase of Y atoms not only leads to the change of each phase content, but causes the lattice distortion. The z -Axis length c of Mg_2Ni lattice increases with the increase of Y content. Comparing with the as-cast $\text{Mg}_{67}\text{Ni}_{27}\text{Y}_6$ ribbons, the corresponding Bragg peaks of the melt-spun $\text{Mg}_{67}\text{Ni}_{27}\text{Y}_6$ ribbons are broadening and overlapping. Furthermore, the grains are refined and the crystallinity reduces. The melt-spun technique is sufficient to refine the grain of the $\text{Mg}_{67}\text{Ni}_{33-x}\text{Y}_x$ ($x = 0, 1, 3, 6$) alloys, but not sufficient to obtain complete amorphous alloy.

3.2. Microstructures of as-cast $\text{Mg}_{67}\text{Ni}_{33-x}\text{Y}_x$ alloys

Fig. 3 shows the microstructures of the as-cast $\text{Mg}_{67}\text{Ni}_{33-x}\text{Y}_x$ ($x = 0, 1, 3, 6$) alloys, the chemical composition of each phase is summarized in Table 2. As can be seen from Fig. 3(a), the as-cast $\text{Mg}_{67}\text{Ni}_{33-x}\text{Y}_x$ alloy with $x = 0$ is made up of Mg_2Ni , $\alpha\text{-Mg}$ and a small quantity of MgNi_2 . The dendritic matrix A with smooth boundary in Fig. 3(a) is Mg_2Ni phase, white block B is MgNi_2 phase. The regular lamellar structures in gaps of dominant Mg_2Ni phase are the eutectic structures of Mg_2Ni and $\alpha\text{-Mg}$. The microstructure of the as-cast $\text{Mg}_{67}\text{Ni}_{33-x}\text{Y}_x$ alloy with $x = 1$ is shown in Fig. 3(b). It contains Mg_2Ni matrix, eutectic structure of Mg_2Ni and $\alpha\text{-Mg}$ and the white MgNi_2 block distributed in Mg_2Ni matrix. The MgNi_2 phases in the as-cast $\text{Mg}_{67}\text{Ni}_{33-x}\text{Y}_x$ ($x = 0, 1$) alloys are remnants of the incomplete peritectic reaction. In contrast with the $\text{Mg}_{67}\text{Ni}_{33-x}\text{Y}_x$ alloy with $x = 0$, the content of the MgNi_2 phase in

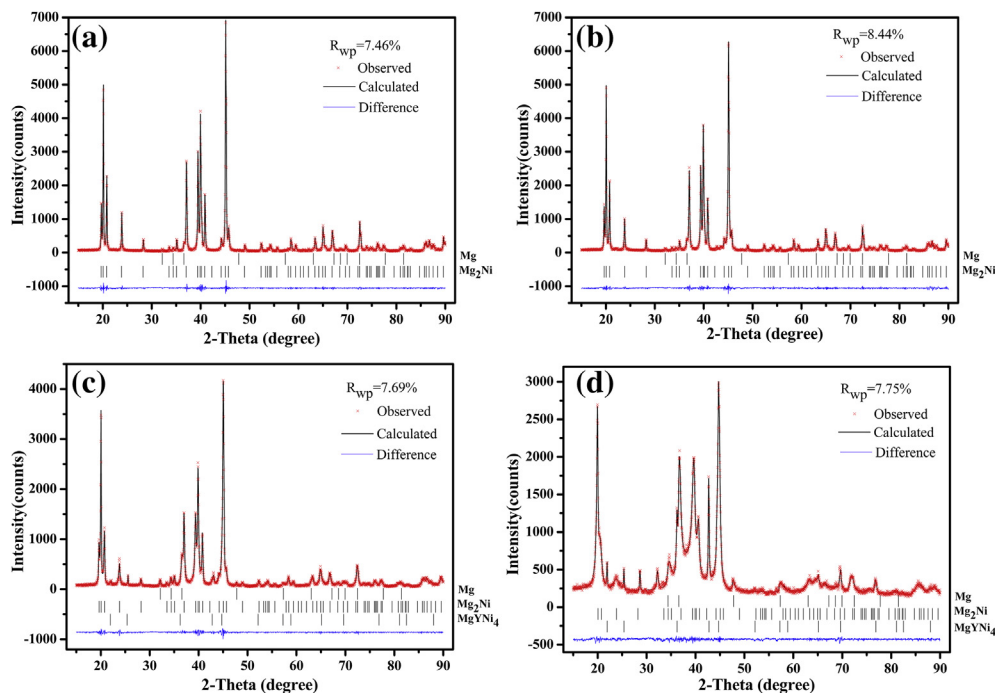


Fig. 2. The Rietveld refinements for the XRD patterns of the melt-spun $\text{Mg}_{67}\text{Ni}_{33-x}\text{Y}_x$ ($x = 0, 1, 3, 6$) ribbons. (a) $x = 0$, (b) $x = 1$, (c) $x = 3$, (d) $x = 6$.

Table 1The lattice parameters and contents of constitute phases of melt-spun $\text{Mg}_{67}\text{Ni}_{33-x}\text{Y}_x$ ($x = 0, 1, 3, 6$) ribbons.

| Sample | | | $x = 0$ | $x = 1$ | $x = 3$ | $x = 6$ |
|--------------------|------------------------|---------------------|-------------------------------|-------------------------------|-------------------------------|-------------------------------|
| Constituent phases | Mg_2Ni | Space group | P6222 | P6222 | P6222 | P6222 |
| | | Lattice periods (Å) | $a = 5.2073$ $c = 13.2378$ | $a = 5.2124$ $c = 13.2549$ | $a = 5.2171$ $c = 13.2706$ | $a = 5.1487$ $c = 13.4929$ |
| | | Unit cell volume | 310.87 | 311.88 | 312.81 | 309.76 |
| | | Contents (wt. %) | 97.4 | 95.8 | 92.8 | 88.5 |
| | Mg | Space group | P63/mmc | P63/mmc | P63/mmc | P63/mmc |
| | | Lattice periods (Å) | $a = 3.2260$ $c = 5.2089$ | $a = 3.2291$ $c = 5.2122$ | $a = 3.2275$ $c = 5.2081$ | $a = 3.2224$ $c = 5.2220$ |
| | | Unit cell volume | 46.95 | 47.07 | 46.98 | 46.96 |
| | | Contents (wt. %) | 2.6 | 4.2 | 4.7 | 7.3 |
| | MgYNi_4 | Space group | — | — | F-43m | F-43m |
| | | Lattice periods (Å) | — | — | $a = 6.9714$ | $a = 7.0188$ |
| | | Unit cell volume | — | — | 338.81 | 345.77 |
| | | Contents (wt. %) | — | — | 2.5 | 4.2 |

the alloy with $x = 1$ increases obviously. The chemical composition of MgNi_2 phase is analyzed by EDS and the results are shown in Table 2. It is found that Y atoms are mainly soluted in MgNi_2 phase. The microstructure of the as-cast $\text{Mg}_{67}\text{Ni}_{33-x}\text{Y}_x$ ($x = 3$) can be seen in Fig. 3(c). The as-cast $\text{Mg}_{67}\text{Ni}_{33-x}\text{Y}_x$ alloy with $x = 3$ contains Mg_2Ni matrix, eutectic structure of Mg_2Ni and α -Mg and a small quantity of white MgYNi_4 phase (B in Fig. 3(c)). The insert figure in Fig. 3(c) is low-magnification image of the as-cast $\text{Mg}_{67}\text{Ni}_{33-x}\text{Y}_x$ alloy with $x = 3$. The Mg_2Ni matrix present typical dendrite, the secondary arm spacing is around $25.4 \mu\text{m}$. The interface of Mg_2Ni dendrite phase is jagged, the Mg_2Ni shows typical facet. The eutectic structure in the alloy with $x = 3$ is much finer than that of the alloys with $x = 0$ and 1. The eutectic structure is not entire regular lamellar, the directions of eutectics lamellas are perpendicular to the interface of Mg_2Ni phase boundary. The eutectic lamellas stop growing when they are collided, the center structure of eutectics lamellar is retained as reticulation. Fig. 3(d) shows the microstructure of the as-cast $\text{Mg}_{67}\text{Ni}_{33-x}\text{Y}_x$ alloy with $x = 6$. The white phase A is confirmed as MgYNi_4 phase from the results of

XRD and EDS. The morphology of MgYNi_4 shows regular triangle, trapezoid, quadrangle and rectangle as they are cross sections of random tetrahedron. Gray stripe phase B is Mg_2Ni , which contains a few Y atoms. D and E are the eutectic structure of α -Mg and Mg_2Ni with soluted Y atoms, the EDS results are shown in Table 2. The eutectic microstructure is needlelike, which also can be seen in the work of Kalinichenka [5]. Black phase E distributes between Mg_2Ni phase and eutectic microstructure is α -Mg, and the shape is irregular. The black α -Mg phase is considered to be last solidified. Trace Y atoms are detected in the last solidified α -Mg phase. As can be seen from the microstructures of the as-cast $\text{Mg}_{67}\text{Ni}_{33-x}\text{Y}_x$ ($x = 0, 1, 3$) alloy, the phase boundary of Mg_2Ni phase changes from smooth to jagged considering the constitutional undercooling during solidification process increases with increasing Y content [29].

3.3. Microstructures of melt-spun $\text{Mg}_{67}\text{Ni}_{33-x}\text{Y}_x$ ribbons

The microstructures of the melt-spun $\text{Mg}_{67}\text{Ni}_{33-x}\text{Y}_x$ ($x = 0, 1, 3, 6$) ribbons are shown in Fig. 4. Comparing with the as-cast

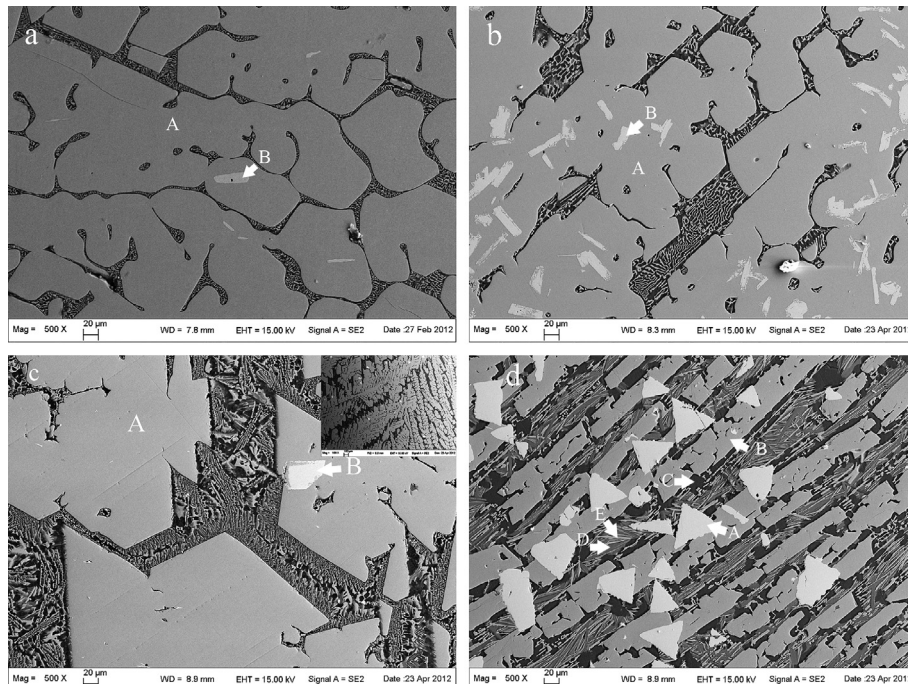


Fig. 3. The microstructures of the as-cast $\text{Mg}_{67}\text{Ni}_{33-x}\text{Y}_x$ ($x = 0, 1, 3, 6$) alloys. (a) $x = 0$, (b) $x = 1$, (c) $x = 3$, (d) $x = 6$.

Table 2The EDS result of as-cast $\text{Mg}_{67}\text{Ni}_{33-x}\text{Y}_x$ ($x = 0, 1, 3, 6$) alloys.

| Fig | Position | Atomic percent (%) | | |
|------|----------|--------------------|-------|-------|
| | | Mg | Ni | Y |
| 3(a) | A | 68.38 | 31.62 | |
| | B | 37.51 | 62.49 | |
| 3(b) | A | 67.64 | 32.36 | |
| | B | 30.29 | 63.18 | 6.53 |
| 3(c) | A | 68.06 | 31.94 | |
| | B | 27.85 | 63.16 | 8.99 |
| 3(d) | A | 18.82 | 62.77 | 18.41 |
| | B | 67.82 | 31.14 | 1.04 |
| | C | 99.41 | 0.59 | |
| | D | 91.85 | 3.46 | 4.69 |
| | E | 66.01 | 31.02 | 2.96 |

$\text{Mg}_{67}\text{Ni}_{33-x}\text{Y}_x$ ($x = 0, 1, 3, 6$) alloys, the grains of the melt-spun $\text{Mg}_{67}\text{Ni}_{33-x}\text{Y}_x$ ($x = 0, 1, 3, 6$) ribbons are much finer. As can be seen in Fig. 4(a), the microstructure of the melt-spun $\text{Mg}_{67}\text{Ni}_{33-x}\text{Y}_x$ ribbons with $x = 0$ is dendritic. The grain size is statistically measured by a quantitative metallography method. The secondary dendrite arm spacing (SDAS) of the melt-spun $\text{Mg}_{67}\text{Ni}_{33-x}\text{Y}_x$ ribbons with $x = 0$ is around $2.3 \mu\text{m}$, while the SDAS of the corresponding as-cast alloy is around $82.8 \mu\text{m}$. The microstructure of the melt-spun $\text{Mg}_{67}\text{Ni}_{33-x}\text{Y}_x$ ribbons with $x = 1$ is shown in Fig. 4(b), the microstructure is also dendritic, the average SDAS is around $6.5 \mu\text{m}$, while the average SDAS of the as-cast $\text{Mg}_{67}\text{Ni}_{33-x}\text{Y}_x$ alloy with $x = 1$ is around $63.6 \mu\text{m}$. Fig. 4(c) shows the microstructure of the melt-spun $\text{Mg}_{67}\text{Ni}_{33-x}\text{Y}_x$ ribbons with $x = 3$, the microstructure is lath-shaped and the white phase is MgYNi_4 . The average width of lath is around $2.0 \mu\text{m}$, and the length is around $8.7 \mu\text{m}$. The corresponding as-cast $\text{Mg}_{67}\text{Ni}_{33-x}\text{Y}_x$ alloy with $x = 3$ shows typical dendritic morphology, the length of primary dendrite arm is above

$1700 \mu\text{m}$, the SDAS is around $25.4 \mu\text{m}$. The black area in the microstructures of the melt-spun $\text{Mg}_{67}\text{Ni}_{33-x}\text{Y}_x$ ($x = 0, 1, 3$) ribbons is considered to be a shrinkage porosity, which can be attributed to the rapid solidification in melt-spun process. The pores percentage in the melt-spun $\text{Mg}_{67}\text{Ni}_{33-x}\text{Y}_x$ ($x = 0, 1, 3$) ribbons are $\sim 12\%$, $\sim 14\%$ and $\sim 11\%$, respectively. The pores can act as hydrogen storage position and hydrogen atoms diffusion channels [30], which are beneficial to improve the hydrogen absorption capacity and kinetics of the alloys. The pores are connected to each other in $\text{Mg}_{67}\text{Ni}_{32}\text{Y}$ alloy and the connected pores are favorable for the hydrogen atoms diffusion. The microstructure of the melt-spun $\text{Mg}_{67}\text{Ni}_{33-x}\text{Y}_x$ ribbons with $x = 6$ is shown in Fig. 4(d), the matrix phase is continuous Mg_2Ni nanocrystalline with a small quantity of amorphous, and the white phase is MgYNi_4 . However, no pores are found in the microstructure of the melt-spun $\text{Mg}_{67}\text{Ni}_{33-x}\text{Y}_x$ ribbons with $x = 6$. Probably because the liquid metal viscosity increases with the addition of Y. Combining with the results of XRD, the crystallinity decreases and nanocrystalline forms in the melt-spun $\text{Mg}_{67}\text{Ni}_{33-x}\text{Y}_x$ ribbons with $x = 6$.

3.4. Activation of melt-spun $\text{Mg}_{67}\text{Ni}_{33-x}\text{Y}_x$ ribbons

In order to remove the oxide and/or hydroxide surface contamination, the metal-based hydrogen storage materials are always needed to be activated prior to the formal measurements [21,24,31]. The activation of the alloys in this work is achieved through three successive absorption/desorption cycles [6]. Fig. 5 demonstrates kinetics of the initial hydrogen absorption in the melt-spun $\text{Mg}_{67}\text{Ni}_{33-x}\text{Y}_x$ ($x = 0, 1, 3, 6$) ribbons under the initial hydrogen pressure 30 bar at 623 K. No incubation period is observed in the melt-spun $\text{Mg}_{67}\text{Ni}_{33-x}\text{Y}_x$ ribbons with $x = 0$, while the incubation period is observed in the melt-spun $\text{Mg}_{67}\text{Ni}_{33-x}\text{Y}_x$ ribbons with $x = 1, 3$ and 6 as shown in Fig. 5. With the addition of Y,

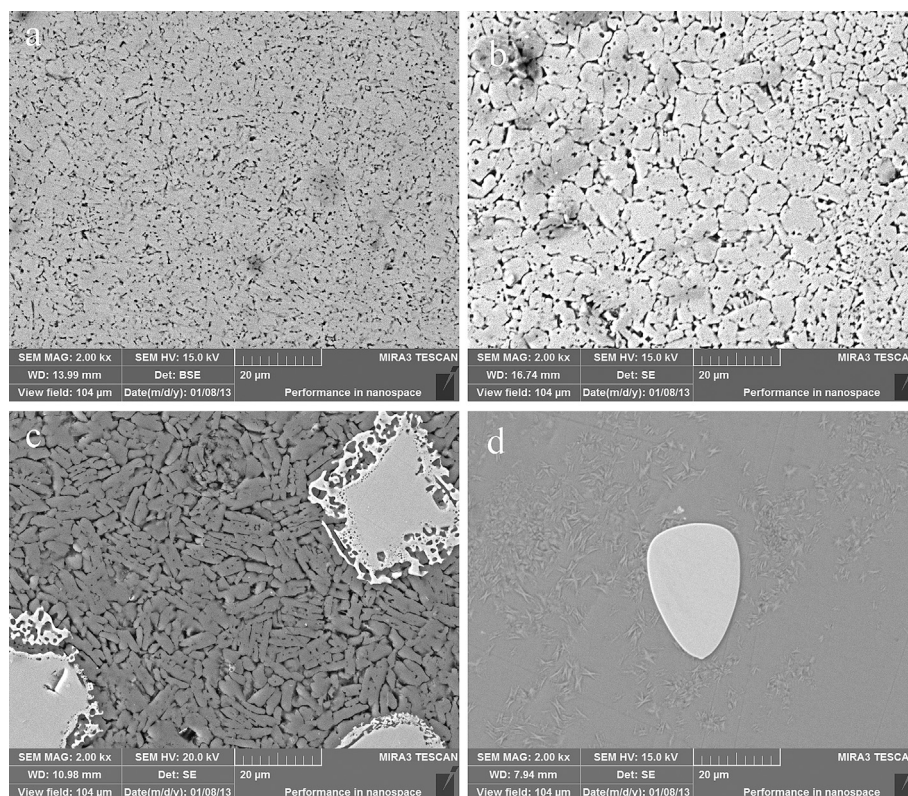


Fig. 4. The microstructures of the melt-spun $\text{Mg}_{67}\text{Ni}_{33-x}\text{Y}_x$ ($x = 0, 1, 3, 6$) ribbons. (a) $x = 0$, (b) $x = 1$, (c) $x = 3$, (d) $x = 6$.

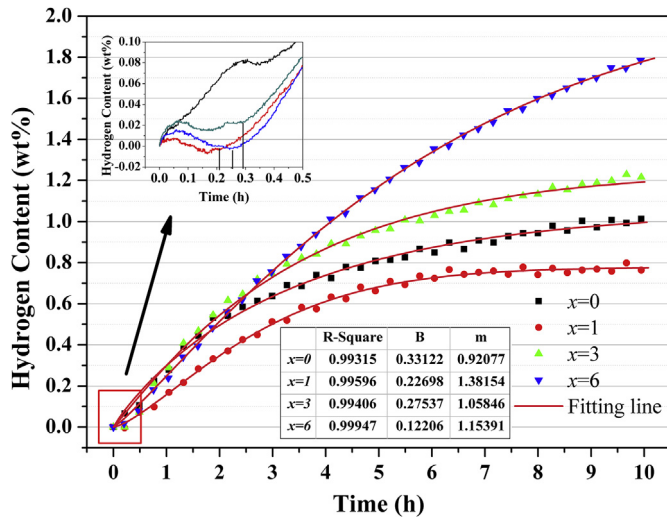


Fig. 5. The kinetics of the initial hydrogen absorption in the $\text{Mg}_{67}\text{Ni}_{33-x}\text{Y}_x$ ($x = 0, 1, 3, 6$) melt-spun ribbons under 30 bar at 623 K.

the length of incubation period increases. The incubation time is generally related to the surface properties of the alloy [32], metallic oxide prevents the hydrogen dissociation. The increase of the incubation period time may be attributed to the increase of Y content. The initial hydrogen absorption capacities of the melt-spun $\text{Mg}_{67}\text{Ni}_{33-x}\text{Y}_x$ ($x = 0, 1, 3, 6$) ribbons are 1.00, 0.78, 1.22 and 1.81 wt. %, respectively. With the addition of Y, the initial hydrogen absorption capacity decreases for the alloy with $x = 1$. As the content of Y further increases to $x = 3$ and 6, the hydrogenation capacity significantly increases. The melt-spun $\text{Mg}_{67}\text{Ni}_{33-x}\text{Y}_x$ ribbons with $x = 3$ and 6 reveal a fast hydrogenation rate and high capacity comparing with that of the melt-spun $\text{Mg}_{67}\text{Ni}_{33-x}\text{Y}_x$ ribbons with $x = 0$. The fast hydrogenation rate and high capacity can be attributed to the refined grain size, as well as related to the MgYNi_4 phase. The hydrides formation enthalpy of MgYNi_4 has been calculated to be $-35.8 \text{ kJ mol}^{-1} \text{ H}_2$ [28], the absolute value is relatively low in comparison with that of the other Mg-based hydrides (i.e. $\Delta H[\text{MgH}_2] \approx -74 \text{ kJ mol}^{-1} \text{ H}_2$, $\Delta H[\text{Mg}_2\text{NiH}_4] \approx -65 \text{ kJ mol}^{-1} \text{ H}_2$) [33]. It has been reported that the MgYNi_4 is a material with low hydrogen absorption/desorption temperature and the MgYNi_4 has a significant catalytic effects on MgH_2 [34]. In addition, the nanocrystalline and amorphous microstructure in the melt-spun $\text{Mg}_{67}\text{Ni}_{33-x}\text{Y}_x$ ribbons with $x = 6$ contains plenty of defects which enhance the hydrogen diffusivity, and the amorphous leads to an easier access of hydrogen to nanocrystallines avoiding the long-range diffusion of hydrogen atoms through an already formed hydrides [35]. However, the amorphous will be crystallized after several times absorption/desorption cycles, the superiority are no longer obvious in later absorption/desorption processes.

Much effort has been strived to the hydriding of metals, and several hydriding mechanisms have been proposed. A typical one is nucleation and growth process based on the Avrami-Erofeev equation Eq. (1) [36,37].

$$\alpha = 1 - \exp(-Bt^m) \quad (1)$$

where α is the reaction rate, meaning the ratio of reacted material, t is reaction time, B and m are constants. The observed hydrogenation rate curves fit to the typical nucleation and growth process well, and the fitted R-square values are shown in Fig. 5. The hydrogenation of Mg particles are a nucleation, growth and

impingement processes [38]. The hydrides nucleate at the surface of particles, then the hydrides grow and connect with each other when they are impinged. The initial hydrogen absorption of the melt-spun $\text{Mg}_{67}\text{Ni}_{33-x}\text{Y}_x$ ribbons are considered as nucleation and growth processes [39].

The hydride nucleation always takes place at defects including grain boundaries [38] and lattice distortion locations. In the activation process, plenty of fine grains of melt-spun alloys and the nanocrystalline/amorphous microstructure provide abundant nucleation sites and hydrogen diffusion paths. The diffusion paths are opened gradually in absorption/desorption cycling process. As a result, hydrogen atoms can diffuse rapidly through these paths. The pores caused by the melt-spun technique increase the surfaces area, which increases the difficulty to be activated and slightly decreases the initial hydrogenation content of the melt-spun $\text{Mg}_{67}\text{Ni}_{33-x}\text{Y}_x$ ribbons with $x = 1$. The surface activity of the pores increases after several hydrogenation/dehydrogenation cycles. The hydrogenation rate and capacity of the melt-spun $\text{Mg}_{67}\text{Ni}_{33-x}\text{Y}_x$ ($x = 0, 1, 3$) ribbons increase rapidly with the increased activated surfaces after several hydrogenation/dehydrogenation cycles. The pores in melt-spun alloys are important hydrogen diffusion channels and storage sites. After activated for 3 absorption/desorption cycles, the hydrogen absorption capacities of melt-spun $\text{Mg}_{67}\text{Ni}_{33-x}\text{Y}_x$ ($x = 0, 1, 3, 6$) ribbons at 623 K reach approximately 2.78, 3.59, 3.35 and 3.25 wt. %, respectively.

3.5. Hydrogenation properties of melt-spun $\text{Mg}_{67}\text{Ni}_{33-x}\text{Y}_x$ ribbons

Fig. 6(a) shows the hydrogenation behavior of the activated melt-spun $\text{Mg}_{67}\text{Ni}_{33-x}\text{Y}_x$ ($x = 0, 1, 3, 6$) ribbons under initial H_2 pressure 30 bar at 573 K. It is clear that the hydrogen content reaches maximum after hydrogenating for 4 h. The maximum hydrogen storage capacity of the melt-spun $\text{Mg}_{67}\text{Ni}_{33-x}\text{Y}_x$ ($x = 0, 1, 3, 6$) ribbons at 573 K is 3.15, 3.79, 3.78 and 3.45 wt. %, respectively. With the addition of Y, the hydrogen storage capacities of the melt-spun $\text{Mg}_{67}\text{Ni}_{33-x}\text{Y}_x$ ($x = 1, 3, 6$) ribbons increase significantly comparing with that of the melt-spun ribbons without Y. It can be observed that the hydrogen absorption rates of the melt-spun $\text{Mg}_{67}\text{Ni}_{33-x}\text{Y}_x$ ($x = 0, 1, 3, 6$) ribbons increase with the increase of Y content. The curves can be divided into two stages, rapid hydrogen absorption stage (linear part of the curve) and stable hydrogen absorption stage (bending part of the curve). The amount of hydrogen absorption for the melt-spun $\text{Mg}_{67}\text{Ni}_{33-x}\text{Y}_x$ ($x = 0, 1, 3, 6$) ribbons within 30 s (linear part of the curve) are more than 60% of the maximum hydrogen absorption capacity. As mentioned above, the grain size is significantly refined and the grain boundaries increase by melt-spun. Meanwhile, the pores provide increased diffusion channels and hydrogen storage sites. Therefore, the melt-spun ribbons can be expected to absorb abundant hydrogen atoms rapidly. The kinetics curves are plotted by fitting Avrami-Erofeev equation (Eq. (1)) in Fig. 6(a). The fitting curves are well agreed with the experimental data. The nucleation and growth of the hydrides in hydrogen absorption process are controlled by diffusion [39]. These hydrogenation curves characteristics might be explained by the fact that a surface-near hydrides layer is formed within the first seconds, therefore, the diffusion of hydrogen atoms through this layer becomes the rate-limiting factor [40]. With the increase of hydrides layer thickness, the diffusion of hydrogen through the hydrides layer is more difficult, the hydrogenation rate further decreases. The lattice distortion caused by the addition of Y element is believed to be positive for the hydrogenation kinetics. As a result, the hydrogen absorption rates of melt-spun $\text{Mg}_{67}\text{Ni}_{33-x}\text{Y}_x$ ($x = 1, 3, 6$) ribbons are higher than that of the alloy with $x = 0$. The hydrogenation capacity of the melt-spun $\text{Mg}_{67}\text{Ni}_{33-x}\text{Y}_x$ ribbons with $x = 6$ slightly decreases comparing with the alloys $x = 1$ and 3. It can be explained by two

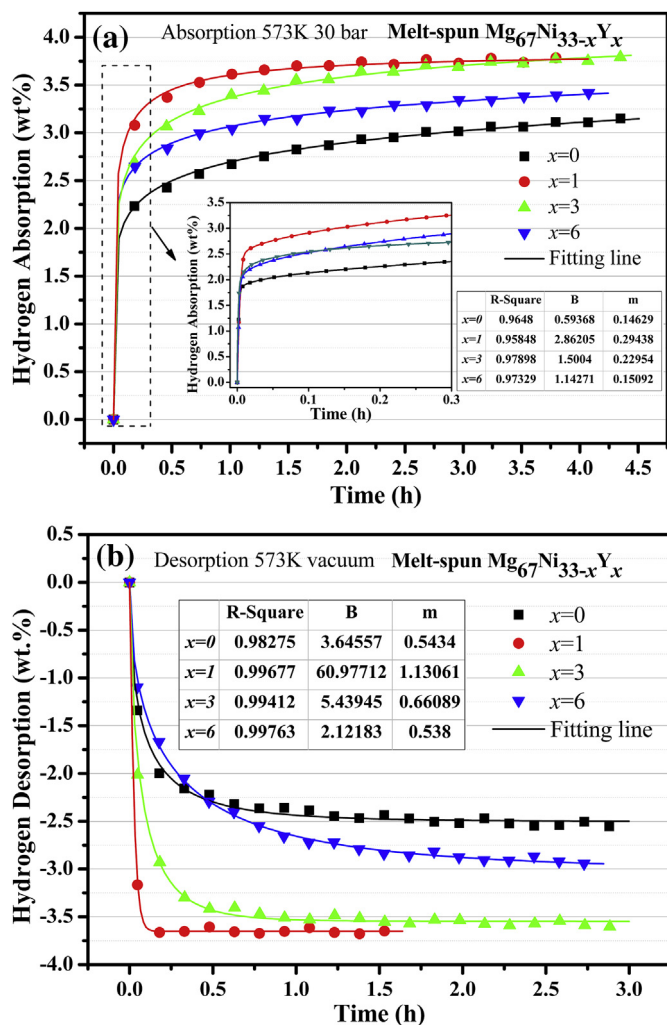


Fig. 6. The hydrogen storage property of the activated melt-spun $Mg_{67}Ni_{33-x}Y_x$ ($x = 0, 1, 3, 6$) ribbons. (a) The hydrogenation behavior under initial H_2 pressure 30 bar at 573 K; (b) the dehydrogenation behavior under initial vacuum at 573 K.

reasons, one is the absence of pores which can provide hydrogen storage sites, the other is the existence of the $MgYNi_4$ phase with low hydrogenation capacity [28]. But $MgYNi_4$ reveals significantly catalytic effect on initial hydrogenation as mentioned above. The pores in melt-spun $Mg_{67}Ni_{33-x}Y_x$ ribbons with $x = 1$ increase the hydrogen diffusion channels and hydrogen storage sites. In addition, the $MgNi_2$ phase without hydrogen absorption capacity and the low hydrogenation capacity $MgYNi_4$ phase are not formed in the melt-spun $Mg_{67}Ni_{33-x}Y_x$ ribbons with $x = 1$. As a result, the melt-spun $Mg_{67}Ni_{33-x}Y_x$ ribbons with $x = 1$ possess high hydrogen storage capacity and fast hydrogen absorption kinetics.

The phase compositions of the hydrogenated melt-spun $Mg_{67}Ni_{33-x}Y_x$ ($x = 0, 1, 3, 6$) ribbons have been characterized by XRD. The Mg_2NiH_4 phase with monoclinic structure is dominant phase. Several Bragg peaks of the MgH_2 phase and the $Mg_2NiH_{0.3}$ phase are observed in the XRD patterns of the hydrogenated melt-spun $Mg_{67}Ni_{33-x}Y_x$ ($x = 0, 1, 3$) ribbons. The Mg_2NiH_4 and the MgH_2 phases are the saturated hydrides of the Mg_2Ni and α -Mg, respectively. The $Mg_2NiH_{0.3}$ phase is the unsaturated hydride phase of Mg_2Ni phase. The content of MgH_2 increases with the increase of Y. Because the content of α -Mg in the melt-spun $Mg_{67}Ni_{33-x}Y_x$ ($x = 0, 1, 3, 6$) ribbons increases with increasing Y. Due to increased pores and the catalysis of the $MgYNi_4$ [34], the unsaturated hydride

$Mg_2NiH_{0.3}$ phase decreases with the increase of Y. For the hydrogenated melt-spun $Mg_{67}Ni_{33-x}Y_x$ ribbons with $x = 6$, two different Mg_2NiH_4 phases with monoclinic and cubic structure are detected. The Bragg peaks of YH_2 and YH_3 phases are also observed in addition to the two Mg_2NiH_4 phases, $Mg_2NiH_{0.3}$ and MgH_2 phases. The existence of unsaturated hydride $Mg_2NiH_{0.3}$ phase indicates that the melt-spun $Mg_{67}Ni_{33-x}Y_x$ ($x = 0, 1, 3, 6$) ribbons are not hydrogenated completely. Y hydride is formed after yttrium inter-metallic exposed to the hydrogen gas [41]. The YH_3 provides special sites and paths to facilitate the decomposition of H_2 to H atom and helps the H atom diffusing through Mg and MgH_2 [42]. It has been reported that the maximum hydrogen desorption peak from the transformation of YH_3 into YH_2 occurs at 553 K [43], which is lower than Mg_2Ni . The YH_3 phases play an important role in improving hydrogen absorption/desorption kinetics of Mg_2Ni .

Fig. 6(b) shows the dehydrogenation behavior of the melt-spun $Mg_{67}Ni_{33-x}Y_x$ ($x = 0, 1, 3, 6$) ribbons in initial vacuum at 573 K. The amount of hydrogen desorption are 2.50, 3.65, 3.55 and 2.95 wt. %, respectively. They are 79%, 96%, 94% and 86% of the corresponding maximum hydrogen absorption capacity. The higher of the hydrogen absorption capacity ensures the large the hydrogen desorption capacity, but all the experimental alloys are dehydrogenated incompletely. The time to desorption equilibrium of the melt-spun $Mg_{67}Ni_{33-x}Y_x$ ($x = 0, 1, 3, 6$) ribbons is 100, 8, 60 and 160 min, respectively. The hydrogen desorption behavior fits the Avrami-Erofeev equation (Eq. (1)) well and the corresponding m values are shown in Fig. 6(b). The hydrogen desorption of each melt-spun $Mg_{67}Ni_{33-x}Y_x$ ($x = 0, 1, 3, 6$) alloy follows the diffusion controlled nucleation and growth process. The pores and the defects including grain boundaries and lattice distortion increase the sites of the nucleation. Meanwhile, the pores can act as the fast-diffusion channels that hydrogen atoms can release from the metal. The melt-spun $Mg_{67}Ni_{33-x}Y_x$ alloy with $x = 1$ reveals high hydrogen desorption rate and capacity for the interconnected pores. The lattice distortion and the pores not only raise the hydrogen absorption/desorption rate, but significantly improve the hydrogen storage capacities of $Mg_{67}Ni_{33-x}Y_x$ ($x = 0, 1, 3, 6$) alloys.

4. Conclusions

In summary, microstructures and hydrogen storage properties of the $Mg_{67}Ni_{33-x}Y_x$ ($x = 0, 1, 3, 6$) alloys are investigated in this work. It is found as-cast $Mg_{67}Ni_{33-x}Y_x$ ($x = 0, 1, 3, 6$) alloys preserve multiphase structures. The as-cast $Mg_{67}Ni_{33-x}Y_x$ alloys with $x = 0$ and 1 contain Mg_2Ni , α -Mg and $MgNi_2$ phases. For the as-cast $Mg_{67}Ni_{33-x}Y_x$ alloys with $x = 3$ and 6, $MgYNi_4$ phase with C15b ($AuBe_5$)-type Laves phase structure is observed in addition to Mg_2Ni and α -Mg. The phase compositions in melt-spun $Mg_{67}Ni_{33-x}Y_x$ ribbons are almost the same as the as-cast $Mg_{67}Ni_{33-x}Y_x$ alloys apart of $MgNi_2$ phase. The rapid solidification process of melt-spun results in shrinkage porosity in the $Mg_{67}Ni_{33-x}Y_x$ ($x = 0, 1, 3$) alloys and nanocrystalline/amorphous in the $Mg_{67}Ni_{33-x}Y_x$ alloy with $x = 6$. The refined grain size, $MgYNi_4$ and nanocrystalline/amorphous improve the initial hydrogenation rate and capacity of melt-spun $Mg_{67}Ni_{33-x}Y_x$ alloys. The pores result in the increase of the area of the contamination to activate, but the pores reveal positive effect to the hydrogen diffusion in the activated melt-spun ribbons. The activated melt-spun $Mg_{67}Ni_{33-x}Y_x$ ($x = 0, 1, 3, 6$) ribbons can absorb 60% maximum capacity within 30 s. The initial hydriding of the melt-spun $Mg_{67}Ni_{33-x}Y_x$ ($x = 0, 1, 3, 6$) ribbons is an nucleation and growth process. The hydrogen absorption and desorption of the activated melt-spun ribbons with various compositions of $Mg_{67}Ni_{33-x}Y_x$ ($x = 0, 1, 3, 6$) are diffusion controlled nucleation and growth processes. The defects, including the grain boundaries and lattice distortions, and the pores provide increased the nucleation

sites, fast-diffusion channels and hydrogen storage locations. The lattice distortion caused by the addition of Y element and the shrinkage porosity by melt-spun not only raise the hydrogen absorption/desorption rate, but significantly improve the hydrogen storage capacity of $\text{Mg}_{67}\text{Ni}_{33-x}\text{Y}_x$ ($x = 0, 1, 3, 6$) alloys.

Acknowledgments

This work is financially supported by the National Defense Basic Scientific Research Project (A2720110010) and Doctorate Foundation of Northwestern Polytechnical University (CX201107). The 111 project (No. B08040) is also acknowledged. Prof. Zhong-min Wang from Guilin University of Electronic Technology is gratefully appreciated for his help in hydrogenation measurements.

References

- [1] I.P. Jain, *Int. J. Hydrogen Energy* 34 (2009) 7368–7378.
- [2] E. David, *J. Mater. Process. Technol.* 162 (2005) 169–177.
- [3] L. Schlapbach, A. Züttel, *Nature* 414 (2001) 353–358.
- [4] B. Sakintuna, F. Lamari-Darkrim, M. Hirscher, *Int. J. Hydrogen Energy* 32 (2007) 1121–1140.
- [5] S. Kalinichenka, L. Rontzsch, T. Riedl, T. Weißgärber, B. Kieback, *Int. J. Hydrogen Energy* 36 (2011) 10808–10815.
- [6] S. Bouaricha, J.P. Dodelet, D. Guay, J. Huot, R. Schulz, *J. Alloys Compd.* 325 (2001) 245–251.
- [7] D.H. Xie, P. Li, C.X. Zeng, J.W. Sun, X.H. Qu, *J. Alloys Compd.* 478 (2009) 96–102.
- [8] I.P. Jain, C. Lal, A. Jain, *Int. J. Hydrogen Energy* 35 (2010) 5133–5144.
- [9] A.D. Rud, A.M. Lakhnik, *Int. J. Hydrogen Energy* 37 (2012) 4179–4187.
- [10] S. Pedneault, J. Huot, L. Roué, *J. Power Sources* 185 (2008) 566–569.
- [11] Y. Zhu, Y. Wang, L. Li, *Int. J. Hydrogen Energy* 33 (2008) 2965–2969.
- [12] E. Wirth, D. Milcius, C. Filiou, D. Noréus, *Int. J. Hydrogen Energy* 33 (2008) 3122–3127.
- [13] S. Løken, J.K. Solberg, J.P. Maehlen, R.V. Denys, M.V. Lototsky, B.P. Tarasov, V.A. Yartys, *J. Alloys Compd.* 446–447 (2007) 114–120.
- [14] Y.H. Cho, S. Aminorroaya, H.K. Liu, A.K. Dahle, *Int. J. Hydrogen Energy* 36 (2011) 4984–4992.
- [15] Á. Révész, Á. Kis-Tóth, L.K. Varga, E. Schafner, I. Bakonyi, T. Spassov, *Int. J. Hydrogen Energy* 37 (2012) 5769–5776.
- [16] R.K. Singh, H. Raghubanshi, S.K. Pandey, O.N. Srivastava, *Int. J. Hydrogen Energy* 35 (2010) 4131–4137.
- [17] L.P. Ma, X.D. Kang, H.B. Dai, Y. Liang, Z.Z. Fang, P.J. Wang, P. Wang, H.M. Cheng, *Acta Mater.* 57 (2009) 2250–2258.
- [18] M.Y. Song, J.-L. Bobet, B. Darriet, *J. Alloys Compd.* 340 (2002) 256–262.
- [19] S.-A. Jin, J.-H. Shim, J.-P. Ahn, Y.W. Cho, K.-W. Yi, *Acta Mater.* 55 (2007) 5073–5079.
- [20] J.J. Reilly Jr., R.H. Wiswall Jr., *Inorg. Chem.* 7 (1968) 2254–2256.
- [21] S. Kalinichenka, L. Röntzsch, C. Baetz, B. Kieback, *J. Alloys Compd.* 496 (2010) 608–613.
- [22] C.X. Shang, Z.X. Guo, *Int. J. Hydrogen Energy* 32 (2007) 2920–2925.
- [23] M.Y. Song, C.-D. Yim, S.N. Kwon, J.-S. Bae, S.-H. Hong, *Int. J. Hydrogen Energy* 33 (2008) 87–92.
- [24] Q.A. Zhang, C.J. Jiang, D.D. Liu, *Int. J. Hydrogen Energy* 37 (2012) 10709–10714.
- [25] A.A. Nayeb-Hashemi, J.B. Clark, *Bull. Alloy Phase Diagrams* 6 (1985) 238–244.
- [26] D. Stefanescu, Peritectic solidification, in: *Science and Engineering of Casting Solidification*, Second ed., Springer, US, 2009, pp. 1–17.
- [27] M. Mezbahul-Islam, M. Medraj, *Calphad* 33 (2009) 478–486.
- [28] K. Aono, S. Orimo, H. Fujii, *J. Alloys Compd.* 309 (2000) L1–L4.
- [29] D. Stefanescu, Micro-scale Phenomena and Interface Dynamics, in: *Science and Engineering of Casting Solidification*, second ed., Springer, US, 2009, pp. 1–30.
- [30] K.M. Thomas, *Catal. Today* 120 (2007) 389–398.
- [31] S. Aminorroaya, H.K. Liu, Y. Cho, A. Dahle, *Int. J. Hydrogen Energy* 35 (2010) 4144–4153.
- [32] S. Suwarno, J.K. Solberg, V.A. Yartys, B. Krogh, *J. Alloys Compd.* 509 (Suppl. 2) (2011) S775–S778.
- [33] A. Kamegawa, Y. Goto, R. Kataoka, H. Takamura, M. Okada, *Renew. Energy* 33 (2008) 221–225.
- [34] L. ChitsazKhoyi, S. Raygan, M. Pourabdoli, *Int. J. Hydrogen Energy* 38 (2013) 6687–6693.
- [35] T. Spassov, L. Lyubenova, U. Köster, M.D. Baró, *Mater. Sci. Eng. A* 375–377 (2004) 794–799.
- [36] L.Z. Ouyang, X.S. Yang, H.W. Dong, M. Zhu, *Scr. Mater.* 61 (2009) 339–342.
- [37] S. Vyazovkin, D. Dollimore, *J. Chem. Inf. Comput. Sci.* 36 (1996) 42–45.
- [38] H.Y. Tien, M. Tanniru, C.Y. Wu, F. Ebrahimi, *Scr. Mater.* 62 (2010) 274–277.
- [39] H.-Y. Zhou, X.-X. Lan, Z.-M. Wang, Q.-R. Yao, C.-Y. Ni, W.-P. Liu, *Int. J. Hydrogen Energy* 37 (2012) 13178–13184.
- [40] G. Friedlmeier, M. Groll, *J. Alloys Compd.* 253–254 (1997) 550–555.
- [41] J.L. Bobet, B. Chevalier, M.Y. Song, B. Darriet, J. Etourneau, *J. Alloys Compd.* 336 (2002) 292–296.
- [42] Z. Li, X. Liu, L. Jiang, S. Wang, *Int. J. Hydrogen Energy* 32 (2007) 1869–1874.
- [43] V.A. Yartys, O. Gutfleisch, V.V. Panasyuk, I.R. Harris, *J. Alloys Compd.* 253–254 (1997) 128–133.